

# Ultrastrong coupling of a single artificial atom to an electromagnetic continuum

P. Forn-Díaz,<sup>1</sup> J. J. García-Ripoll,<sup>2</sup> B. Peropadre,<sup>3</sup> M. A. Yurtalan,<sup>4</sup>  
J.-L. Orgiazzi,<sup>4</sup> R. Belyansky,<sup>4</sup> C. M. Wilson,<sup>4,\*</sup> and A. Lupascu<sup>1,\*</sup>

<sup>1</sup>*Institute for Quantum Computing,  
Department of Physics and Astronomy,  
and Waterloo Institute for Nanotechnology,*

*University of Waterloo, Waterloo, N2L 3G1, Canada*

<sup>2</sup>*Instituto de Física Fundamental IFF-CSIC, Madrid 28006, Spain*

<sup>3</sup>*Department of Chemistry and Chemical Biology,  
Harvard University, Cambridge, Massachusetts 02138, United States*

<sup>4</sup>*Institute for Quantum Computing and Electrical and Computer Engineering Department,  
University of Waterloo, Waterloo, N2L 3G1, Canada*

## Abstract

The study of the interaction of light and matter has led to many fundamental discoveries as well as numerous important technologies. Over the last decades, great strides have been made in increasing the strength of this interaction at the single-photon level, leading to a continual exploration of new physics and applications. In recent years, a major achievement has been the demonstration of the so-called strong coupling regime [1, 2], a key advancement enabling great progress in quantum information science. In this work, we demonstrate light-matter interaction over an order of magnitude stronger than previously reported, reaching a new regime of ultrastrong coupling (USC). We achieve this using a superconducting artificial atom tunably coupled to the electromagnetic continuum of a one-dimensional waveguide. For the largest values of the coupling, the spontaneous emission rate of the atom is comparable to its transition frequency. In this USC regime, the conventional quantum description of the atom and light as distinct entities breaks down, and a new description in terms of hybrid states is required [3, 4]. Our results open the door to a wealth of new physics and applications. Beyond light-matter interaction itself, the tunability of our system makes it promising as a tool to study a number of important physical systems such as the well-known spin-boson [5] and Kondo models [6].

---

\* These authors contributed equally to this work.

Light propagating in a one-dimensional (1D) waveguide is described by a 1D electromagnetic field with a continuous spectrum of frequencies. The strong coupling regime [7] between an atom and such an electromagnetic continuum is defined as the regime in which the atom emits radiation predominantly into the waveguide with a rate  $\Gamma_G$  that significantly exceeds the decoherence rate of the atom as well as emission into any other channel. Achieving strong coupling to a continuum is a recent achievement in quantum optics [8]. Strong atom-waveguide coupling has numerous applications such as the development of quantum networks [9] for quantum communication [10] and quantum simulation [11]. This technology, first demonstrated with superconducting qubits in open transmission lines [8, 10, 12, 13], has also been implemented with both neutral atoms [14, 15], and quantum dots [16] in photonic crystal waveguides.

A novel, unexplored regime of light-matter interaction is the ultrastrong coupling (USC) regime, where  $\Gamma_G$  becomes comparable to the atomic transition frequency,  $\Delta$ , that is  $\Gamma_G \sim \Delta$ . This is a general definition also applicable to the case of discrete modes in cavity-QED systems [17]. Most studies involving atom-field interactions are in the regime  $\Gamma_G \ll \Delta$  where the common rotating-wave approximation (RWA) applies. In the USC regime, the RWA breaks down. As a consequence, it becomes difficult to distinguish atom and photon states and the system is better described by hybrid states, with photons dressing the atom even in the ground state [3, 4, 17]. The Markovian approximation also breaks down in the USC regime because the broad qubit linewidth  $\Gamma_G$  implies that the spectral density of the environment seen by the atom is not independent of frequency [18]. The presence of a continuum of modes ultrastrongly coupled to an atom has the additional effect of renormalizing the atomic frequency from the bare value  $\Delta_0$ , which is a generalization of the well-known Lamb shift to arbitrary coupling strengths. These renormalization effects are also central to the well-known spin-boson model [5], which has been used to describe, for example, open quantum systems [19], quantum stochastic resonance [20] and phase transitions in Josephson junctions [21]. Reaching the USC regime would also allow the exploration of fundamental questions in quantum electrodynamics, such as the ultimate limits in light-matter interaction strength, and quantum simulation of relativistic quantum information phenomena [22]. In addition, ultrastrong couplings may have technological applications, such as single- [23] and multi-photon nonlinearities, and broadband single-photon sources [3]. Note that operating in the USC regime in an open system requires

$\Gamma_G/\Delta \sim (g/\Delta)^2 \approx 0.1$ , where  $g$  is the interaction strength, since  $\Gamma_G \sim g^2/\Delta$  is the dominant time-scale of the energy exchange between atom and environment[3]. By contrast, an atom of frequency  $\Delta$  coupled to a single mode of a cavity with coupling  $g_C$  will require the less stringent, yet still challenging,  $(g_C/\Delta)^2 \sim 10^{-2}$  for the RWA to break down [24, 25].

Superconducting qubits are artificial atoms with transitions in the microwave range of frequencies. Recently, flux-type superconducting qubits [26] have been put forward as candidates to reach the USC regime [3, 27], having demonstrated large galvanic couplings to resonators [25] and a large anharmonicity that allows them to remain an effective two-level system when  $\Gamma_G \sim \Delta$ . This is in contrast to other more weakly anharmonic qubits whose transitions would overlap for large enough  $\Gamma_G$ .

Here, we demonstrate ultrastrong coupling of a superconducting flux qubit coupled to an open 1D transmission line via a shared Josephson junction. As predicted [3, 27], we observe that  $\Gamma_G$  scales with the inverse of the coupling junction size. For devices with a small-enough coupling junction we measure  $\Gamma_G \sim \Delta$ , indicating that we reach the USC regime. Our flux qubit has four Josephson junctions. Two junctions are designed with the same area, while the other two have relative areas [28]  $\alpha \sim 0.6$  and  $\beta > 1$ . The flux qubit is galvanically attached to the center line of a 1D coplanar waveguide transmission line (Fig. 1(a)). In order to achieve ultrastrong couplings, we place the  $\beta$ -junction in parallel to the other three (Fig. 1(b)). The coupling to the line is then mainly determined[3, 27] by the matrix element between ground  $|0\rangle$  and excited  $|1\rangle$  qubit states of the superconducting phase operator across the  $\beta$ -junction  $\langle 0|\hat{\varphi}_\beta|1\rangle \equiv \langle \varphi_\beta\rangle$ , which is the dominant contribution to the coupling for  $\beta < 4$ . The coupling can be made tunable by turning the  $\beta$ -junction into a superconducting quantum interference device (SQUID) (Fig. 1(b)). A SQUID consists of two junctions in parallel in a superconducting loop. It behaves like a single junction with an effective size controlled by the magnetic flux,  $\Phi_\beta$ , threading the loop. Changing  $\beta$  also modifies the minimum qubit splitting  $\Delta$ . In order to minimize this effect, we make the SQUID junctions asymmetric, which lowers the sensitivity of  $\Delta$  to  $\Phi_\beta$ .

The experiments are performed by applying a probe field with a variable frequency and recording the transmitted field amplitude and phase on a vector network analyzer. For emission rates  $\Gamma_1/\Delta \ll 1$ , where  $\Gamma_1$  is the total emission rate, and in the presence of thermal excitations, the transmitted coherent scattering amplitude at low driving power is given by

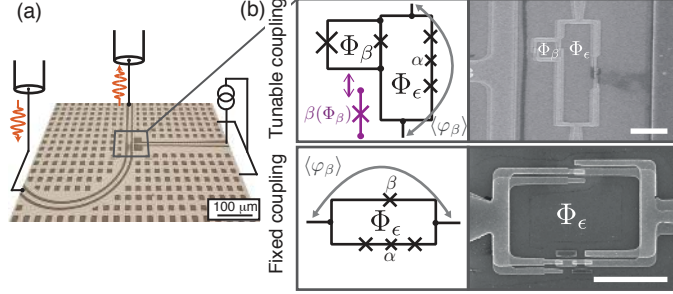


FIG. 1. (a) Schematic of the circuit layout, with a micrograph of a section of a chip containing a transmission line and a flux qubit. (b) Circuit schematic of a flux qubit coupled to a transmission line with tunable (fixed) coupling shown at the top (bottom). In both cases, the coupling is proportional to the matrix element of the phase operator  $\langle \varphi_\beta \rangle$  across the coupling junction. The scanning electron micrographs show the corresponding circuits. The white scale bars are  $4 \mu\text{m}$ .

[29]:

$$T = 1 + R \approx \frac{1 + (\delta\omega/\Gamma_2)^2 + r_0(i\delta\omega/\Gamma_2 - 1)}{1 + (\delta\omega/\Gamma_2)^2}. \quad (1)$$

Here  $\Gamma_2 \equiv \Gamma_\varphi + (\Gamma_1/2)(1 + 2n_{\text{th}})$  is the total decoherence rate,  $\Gamma_\varphi$  is the pure dephasing rate,  $\delta\omega = \omega - \Delta$  is the detuning of the probe field, and  $n_{\text{th}}$  is the thermal photon occupation number at the qubit frequency (Supplementary Information). The maximum reflection amplitude is  $r_0 = \Gamma_1/[2\Gamma_2(1 + 2n_{\text{th}})]$ . As in other experiments on superconducting quantum circuits [8, 10], relaxation into channels other than the waveguide is negligible. Therefore, we assume  $\Gamma_1 = \Gamma_G$ . We note that equation (1) is derived using the RWA, which we expect to break down in the USC regime. However, it has recently been shown [4] that the scattering line shapes are approximately the same in the USC regime up to  $\Gamma_1/\Delta \sim 1$  if we consider  $\Delta$  and  $\Gamma_1$  to be renormalized parameters. This can be shown using a polaron transformation, allowing us to interpret the scattering center as an atom dressed by a cloud of photons.

We first show measurements on a device with a fixed coupling junction with  $\beta \simeq 3.5$  (Fig. 1(b)). The transmission spectrum as a function of applied magnetic field (Fig. 2(a)) shows a maximum extinction at the symmetry point of 95%, indicating strong coupling. By fitting equation 1 (dashed line), we infer  $\Gamma_1/2\pi = 77 \text{ MHz} \ll \Delta/2\pi = 3.996 \text{ GHz}$ , giving  $\Gamma_1/\Delta = 0.02$  which is not in the USC regime. Flux qubit spectra in transmission lines similar to this one have previously been reported [8, 30].

In order to enhance the coupling strength, we designed a second device where the size of

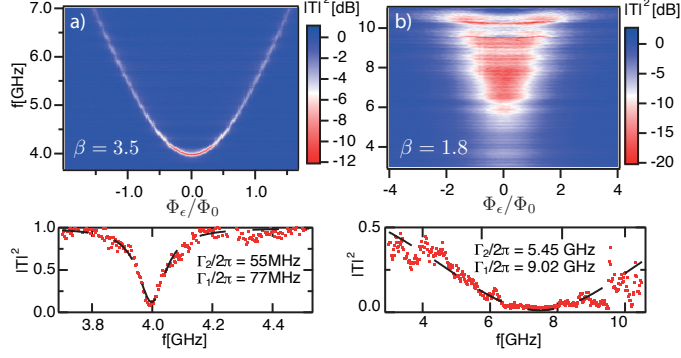


FIG. 2. Spectroscopy of devices with fixed coupling. Top plots show transmission versus frequency and magnetic flux. Bottom plots show transmission corresponding to the magnetic flux at the minimum qubit splitting. Dashed lines are fits to equation (1). (a) Transmission spectrum of qubit with  $\beta \simeq 3.5$  and gap  $\Delta/2\pi = 3.996$  GHz. The 95% extinction on-resonance indicates strong coupling. (b) Spectrum of qubit with  $\beta \simeq 1.8$ . The fit yields  $\Gamma_1/2\pi \simeq 9.02$  GHz, exceeding the qubit gap of  $\Delta/2\pi = 7.7$  GHz. This implies  $\Gamma_1/\Delta = 1.17$ , which indicates ultrastrong coupling.

the  $\beta$ -junction was decreased to  $\beta \simeq 1.8$ . The resulting qubit spectrum in Fig. 2(b) shows striking differences compared to the previous device with  $\beta \simeq 3.5$ . The qubit linewidth at the symmetry point is very large, comparable to the total measurement bandwidth of 3-11 GHz. We infer a full width at half maximum of  $2\Gamma_2/2\pi \simeq 10.9$  GHz. The extracted qubit emission rate  $\Gamma_1/2\pi \simeq 9$  GHz exceeds the qubit splitting  $\Delta/2\pi = 7.7$  GHz, giving  $\Gamma_1/\Delta = 1.2$ , a clear indication that this device reaches the USC regime.

Having observed two devices with  $\Gamma_1 \ll \Delta$  and  $\Gamma_1 > \Delta$ , we now explore the intermediate region using a device with tunable coupling (Fig. 1(b)). The device is designed with a tunable range of  $\beta \sim 1.6 - 3.6$ . The qubit now consists of two loops, the main loop that changes the qubit magnetic energy through the flux  $\Phi_\epsilon$ , and the  $\beta$ -loop that changes the effective coupling to the transmission line through  $\Phi_\beta$  [3]. In the experiment, we sweep the global magnetic field, therefore simultaneously changing  $\Phi_\epsilon$  and  $\Phi_\beta$ . The qubit spectrum shows minima near  $\Phi_\epsilon \approx \Phi_0(1/2 + n)$  with  $\Phi_0 = h/2e$  the quantum of flux,  $n$  being an integer (Supplementary Information). Here, different  $n$  will correspond to different  $\Phi_\beta$ , leading to different coupling strengths. The loop areas  $A_\epsilon/A_\beta$  are designed to have a large, incommensurate ratio, allowing the exploration of many different values of  $\beta$ .

In Figs. 3(a)-(c), spectroscopy of the tunable coupling device is shown at three different values of  $\Phi_\beta$ . Using scanning-electron microscope (SEM) images of the measured device,

we identify Figs. 3(a)-(c) as effectively having, respectively,  $\beta_{(a)} \simeq 3.6$ ,  $\beta_{(b)} \simeq 2.0$ ,  $\beta_{(c)} \simeq 1.6$ . Fig. 3(a) corresponds to the highest effective  $\beta$ -junction size, therefore the lowest coupling strength. A flux qubit spectrum can be identified with  $\Delta/2\pi = 5.2$  GHz and  $2\Gamma_2/2\pi \simeq 2.4$  GHz. The maximum extinction at the symmetry point is over 95%. The quality of the signal below 4 GHz degrades due to the measurement taking place outside the optimal bandwidth of our amplifier and circulators (4-8 GHz, Supplementary Information). In Fig. 3(b), the qubit gap decreases to  $\Delta/2\pi \simeq 2.9$  GHz as expected for a smaller  $\beta$ -junction. The width  $2\Gamma_2/2\pi = 5.9$  GHz is clearly enhanced, with the extinction decreasing to 30%. In Fig. 3(c), the qubit spectrum is barely discernible. The extinction is only 10%, with a response that appears featureless in our frequency range. Figs. 3(d),(e) show the extracted values of  $r_0$  and  $\Gamma_2$  using equation (1).

In order to understand the spectrum of the tunable coupling device and extract the corresponding emission rates  $\Gamma_1$ , we need to take into account finite temperature effects. As discussed in the Methods section, we can set an upper bound on  $n_{\text{th}}$ , which is  $n_{\text{max}} \equiv (1/2)(1/\sqrt{r_0} - 1)$ . Fig. 3(f) shows that all values of  $n_{\text{max}}$  are consistent with a single effective temperature of  $T_{\text{eff}} = 90$  mK, comparable to other superconducting qubit experiments. Using  $0 < n_{\text{th}} < n_{\text{max}}$ , we then put bounds on  $\Gamma_1$ :  $2\Gamma_2 r_0 < \Gamma_1 < 2\Gamma_2 \sqrt{r_0}$ . Using these bounds, we plot  $\Gamma_1/\Delta$  in Fig. 4(a). The plot clearly shows that we can tune the device from the regime of strong coupling all the way into the USC regime. The curves in Fig. 4(a) correspond to the theoretical value of the normalized coupling strength (Supplementary Information)

$$\Gamma_1/\Delta \simeq \frac{1}{8\pi} \frac{R_Q}{Z_0} |\langle \varphi_\beta \rangle|^2, \quad (2)$$

with  $R_Q = h/(2e)^2 = 6.5$  k $\Omega$  the resistance quantum and  $Z_0$  the characteristic impedance of the line. The values of  $|\langle \varphi_\beta \rangle|^2$  are calculated using the methods of reference 3. The observed values of  $\Gamma_1/\Delta$  agree well with the calculated values based on our circuit [3] in a range of impedances close to the nominal 50  $\Omega$ . Including renormalization effects [5] in equation (2) might further improve the agreement with the measurements for  $\beta < 2$ .

Our system allows us to explore the spin-boson (SB) model in an ohmic bath. According to the SB model, the high frequency modes of the transmission line renormalize the bare qubit splitting  $\Delta_0$  to [4, 5]

$$\Delta = \Delta_0 (p\Delta_0/\omega_C)^{\alpha_{\text{SB}}/(1-\alpha_{\text{SB}})}, \quad (3)$$

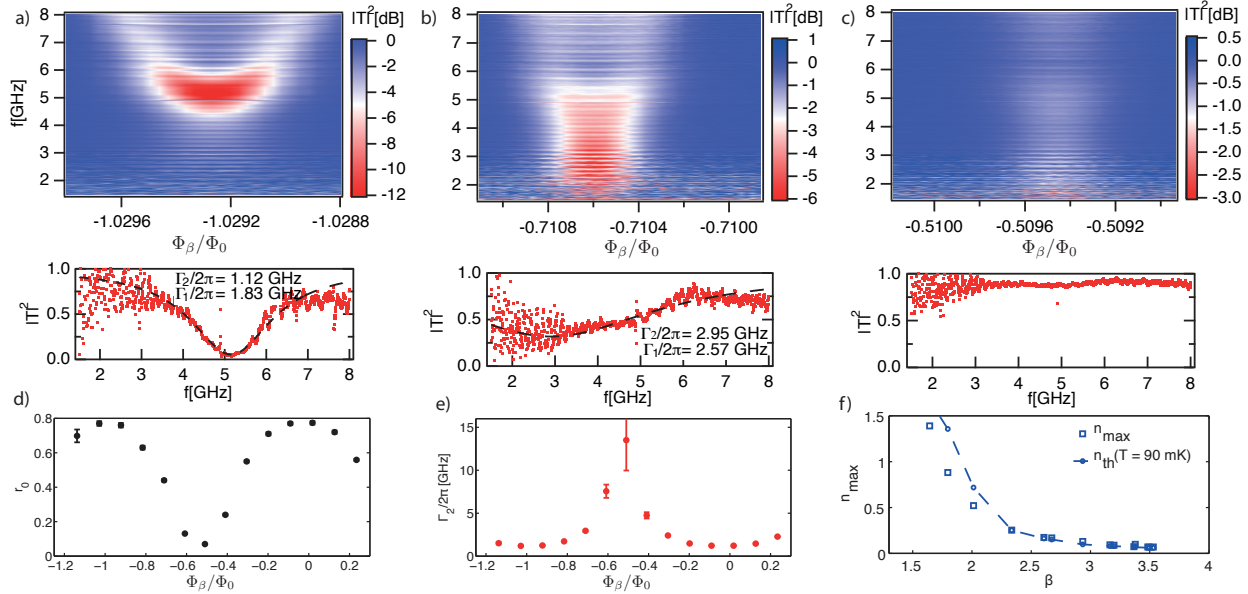


FIG. 3. Tunable ultrastrong coupling. (a-c) Colour plots of transmission versus frequency and magnetic flux (top) and line plots at the magnetic flux corresponding to the minimum qubit splitting (bottom). Dashed lines are fits to equation (1). As a function of the applied magnetic field we observe a transition from strong (a) to ultrastrong coupling (b), (c). (a) For  $\Phi_\beta/\Phi_0 \simeq -1$  the coupling is lowest ( $\beta$  largest) and the extinction is 95% of the transmitted power. (b) At  $\Phi_\beta/\Phi_0 \simeq -0.71$  the qubit reaches  $\Gamma_1 \simeq \Delta$ . (c) Near  $\Phi_\beta/\Phi_0 \simeq -0.5$  the system only reflects 10% of the incoming power and shows little signature of frequency dependence. The measured normalized couplings  $\Gamma_1/\Delta$  are (a) 0.35, (b) 0.90 and (c)  $> 1.5$ , respectively. The large oscillations observed below 4 GHz are caused by reflections outside of our optimal measurement bandwidth 4-8 GHz. (d) Dependence of maximum reflection  $r_0$  on  $\Phi_\beta$ . (e) Modulation of qubit half width at half maximum  $\Gamma_2$  at the symmetry point. From the fits we directly extract  $r_0$  and  $\Gamma_2$ . From these values, we can compute  $\Gamma_1$  and the maximum thermal photon number  $n_{\max}$  (see text) within bounds. (f) Extracted  $n_{\max}$  showing thermal excitation at lower  $\beta$  (lower frequency). It is the decreasing value of  $\Delta$  below  $\sim 5$  GHz that causes the photon occupation to increase exponentially, closely following a thermal distribution at  $T_{\text{eff}} = 90$  mK.

$\alpha_{\text{SB}}$  being the SB normalized coupling strength,  $\omega_C \gg \Delta_0$  the cutoff frequency of the environment and  $p$  is a constant of order 1. We identify  $\alpha_{\text{SB}} = \Gamma_1/\pi\Delta$  (Supplementary Information). In Fig. 4(b) we plot the experimental qubit splittings  $\Delta$  (circles). Using qubit junction dimensions extracted from SEM images of the device, we diagonalize the



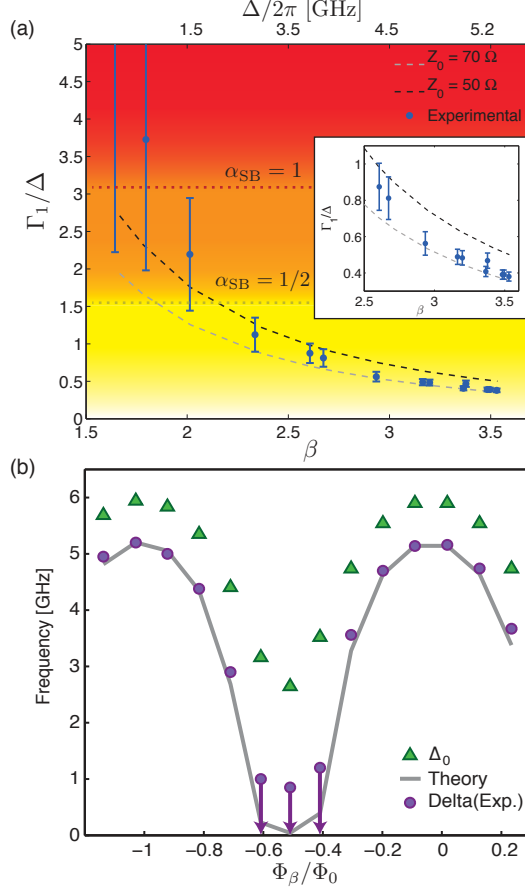


FIG. 4. (a) Experimental normalized coupling rate  $\Gamma_1/\Delta$  (dots) as a function of the coupling junction size  $\beta$ . Error bars correspond to systematic bounds (see text). The curves represent the calculated parameter  $\Gamma_1/\Delta$  from equation (2). There is good agreement with the data for a range of impedances close to the nominal 50  $\Omega$ . The colored regions indicate the spin-boson model regimes where the qubit dynamics are underdamped, overdamped and localized. The inset shows an enlargement of the high- $\beta$  region. (b) Observed qubit frequency  $\Delta$  at the symmetry point (circles) as function of  $\Phi_\beta$ , along with calculated bare qubit gaps  $\Delta_0$  (triangles). The curve is the theoretical prediction for the renormalized qubit gaps calculated using equation 3 assuming a cutoff frequency of  $\omega_C/2\pi = 70$  GHz. Near integers of  $\Phi_\beta/\Phi_0$ , the coupling to the line is minimum and the observed  $\Delta$  follows the shape of the calculated  $\Delta_0$ , with an offset. Near  $\Phi_\beta/\Phi_0 \sim -0.5$ , the difference between  $\Delta$  and  $\Delta_0$  increases substantially. This is the region of ultrastrong coupling and the suppression of  $\Delta$  is consistent with the renormalization effects predicted by the spin-boson model. The spectra in this region are difficult to fit with a Lorentzian and bounds to the frequency indicated by arrows are drawn instead.

qubit Hamiltonian at each flux  $\Phi_\beta$  (triangles) to give the bare qubit gaps  $\Delta_0$ . We then renormalize the calculated  $\Delta_0$  using equation 3 and a value of  $p = \exp(1 + \gamma) \simeq 4.5$ , which is derived using an exponential cutoff model [4, 5].  $\gamma$  is the Euler constant. We find the best fit to the measured  $\Delta$  using a cutoff of  $\omega_C/2\pi = 70$  GHz, which is consistent with characteristic system frequencies such as the plasma frequency of the qubit junctions and the superconducting gap. The agreement between the observed qubit splittings  $\Delta$  and our estimates of the renormalized gaps is clear[3–5].

As a prelude to future work, we can place our results in the context of the SB model. The SB model defines three dynamical regimes for the qubit: underdamped ( $\alpha_{BS} < 0.5$ ), overdamped ( $1 > \alpha_{BS} > 0.5$ ) and localized ( $\alpha_{BS} > 1$ ). The connection between  $\Gamma_1/\Delta$  and  $\alpha_{SB}$  allows us to draw the boundaries between these regimes in Fig. 4(a). We see that our tunable device spans all three regimes. More detailed measurements of the dynamics of the device in these regimes could further confirm the predictions of the SB model. Suggestively, the strong reduction of the qubit response seen in Fig. 3(c) (leftmost data points in Fig. 4(a)) with a flat response as a function of frequency is consistent with simulations of classical double-well dynamics in the overdamped regime (in preparation, P. F.-D.).

We have presented measurements of superconducting flux qubits in 1D open transmission lines in regimes of interaction ranging from strong to ultrastrong coupling. In particular, we observed qubits with emission rates exceeding their own frequency, a clear indication of ultrastrong coupling. These results are very relevant for the study of open systems in the ultrastrong coupling regime, opening the door to the development of a new generation of quantum electronics with ultrahigh bandwidth for quantum and nonlinear optics applications. The tunability of our system also makes it well-suited to the simulation of other quantum systems. In particular, we showed that the device can span the various transition regions of the SB model. With further development of our quantum circuit, the structure of the photon dressing cloud could also be directly detected, allowing the study of physics of the Kondo model [6] in a very well controlled setting. The ultrastrong coupling regime has other interesting intrinsic properties on its own, such as the entangled nature of the ground state.

**Methods** The dependence of  $r_0$  and  $\Gamma_2$  on  $n_{\text{th}}$  shown below equation (1) does not allow the independent extraction of all parameters,  $\Gamma_1, \Gamma_\varphi, n_{\text{th}}$  at each value of  $\beta$ . However, we can set bounds on  $n_{\text{th}}$ . Setting  $\Gamma_\varphi = \Gamma_2(1 - r_0(1 + 2n_{\text{th}})^2) = 0$ , we identify an upper bound on the photon occupation number  $n_{\text{max}} \equiv (1/2)(1/\sqrt{r_0} - 1)$ . If we were to assume  $\Gamma_\varphi/2\pi = 17$  MHz, extracted from the device in Fig. 2(a),  $n_{\text{th}}$  would not differ significantly from the extracted values of  $n_{\text{max}}$  shown in Fig. 3(f). Now, bounds on  $\Gamma_1 = 2\Gamma_2r_0(1 + 2n_{\text{th}})$  can be set as  $\Gamma_1(n_{\text{th}} = 0)$  and  $\Gamma_1(n_{\text{th}} = n_{\text{max}})$  giving  $2\Gamma_2r_0 < \Gamma_1 < 2\Gamma_2\sqrt{r_0}$ . The lower bound,  $n_{\text{th}} = 0$ , is close to the calculated value of  $n_{\text{th}}$  at the cryostat temperature of 10 mK for all qubit frequencies.

**Acknowledgements** We acknowledge financial support from NSERC of Canada, the Canadian Foundation for Innovation, the Ontario Ministry of Research and Innovation, Industry Canada, Canadian Microelectronics Corporation, EU FP7 FET-Open project PROMISCE, Spanish Mineco Project FIS2012-33022 and CAM Network QUITEMAD+. The University of Waterloo's Quantum NanoFab was used for this work. We thank A. J. Leggett and Anupam Garg for fruitful discussions, and M. Otto, S. Chang, A. M. Vaddiraj and C. Deng for help with device fabrication and with the measurement setups.

**Correspondence** Correspondence and requests for materials should be addressed to P. F.-D (email: pfordiaz@uwaterloo.ca), C. M. W. (email: chris.wilson@uwaterloo.ca) or A. L. (email: adrian.lupascu@uwaterloo.ca).

## SUPPLEMENTARY MATERIAL

### S0: DEVICE CHARACTERISTICS AND FABRICATION

The fabrication of devices starts by patterning the transmission line using optical lithography followed by an evaporation of 200 nm of aluminum. A gap in the transmission line is left to place the qubit in a second lithography stage. We pattern the qubit using an electron beam writer. Prior to the second aluminum evaporation an Ar milling step is applied to remove the native oxide on the first aluminum layer, guaranteeing optimal conduction between the two aluminum layers. The qubit is evaporated using double-angle shadow mask evaporation resulting in a total thickness of 105 nm. After the first shadow evaporation step, we oxidize the film with dynamical flow at  $\sim 0.01$  mbar for 7 minutes, yielding critical current densities of  $\sim 12 \mu\text{A}/\mu\text{m}^2$ . The chip is then diced and the transmission line is wire-bonded to a printed circuit board connecting to the rest of the circuitry in our cryostat.

The transmission line consists of a 6.5 mm long on-chip coplanar waveguide with a center line and gaps  $8 \mu\text{m}$  and  $4 \mu\text{m}$  wide, respectively, resulting in a  $50 \Omega$  characteristic impedance. Numerical simulations are run to verify the impedance of the circuit. We use a squared webbed ground to reduce superconducting vortex motion on the ground plane.

Experiments on the device in Fig. 2(a) of the main text and the tunable device were performed in a dilution refrigerator with a base temperature of 9 mK where the chip is thermally anchored to. Our wiring is configured to measure both in reflection as well as in transmission using different input ports, although in this work we only show the transmission measurements. The optimal measurement bandwidth of the system is 4-8 GHz. The on-chip transmission line is followed by two circulators behind a cryogenic amplifier (see Fig. S10 for the full circuit diagram) anchored at 3.2 K with noise temperature of  $\sim 5$  K. We further amplify the signals at room temperature and digitize them using either a vector network analyzer or a spectrum analyzer. The device in Fig. 2(b) of the main text was characterized in a different dilution refrigerator with a base temperature of 15 mK, and having a similar wiring configuration as the one shown in Fig. S10 except for a larger nominal measurement bandwidth of 3-11 GHz.

## S1: QUBIT HAMILTONIAN AND TUNABLE COUPLING OPERATOR

The circuit layout of a flux qubit galvanically tunably coupled to a transmission line with a SQUID-loop shared between the two can be seen in Fig. S1.

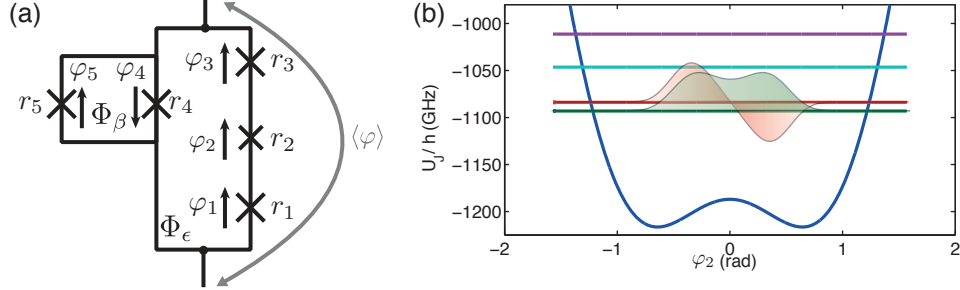


FIG. S1. (a) Schematic of the circuit layout of a flux qubit sharing a SQUID-junction with a transmission line. The coefficients  $r_1, r_2, r_3, r_4, r_5$  represent the relative sizes of the junctions. For the device used in the experiment,  $r_2 = 0.62, r_4 = 2.6, r_2 = r_3 = r_5 = 1$ . (b) Qubit potential with first four energy levels for  $\Phi_\beta = 0, \Phi_\epsilon = \Phi_0/2$  together with the wave functions of the lowest two levels for the ground (symmetric) and first excited state (antisymmetric). The parameters used are similar to the device with tunable coupling of the main text,  $E_J/E_C \simeq 70, E_J/h \simeq 350$  GHz. Notice that the levels lie above the barrier as is usual for flux qubits with level splittings in the GHz range [31].

The Lagrangian of the qubit can be written down by considering the fluxoid quantization condition on the separate loops:

$$\varphi_1 + \varphi_2 + \varphi_3 + \varphi_4 + 2\pi f_\epsilon = 0, \quad (\text{S1})$$

$$\varphi_4 + \varphi_5 + 2\pi f_\beta = 0, \quad (\text{S2})$$

where  $f_\epsilon = \Phi_\epsilon/\Phi_0, f_\beta = \Phi_\beta/\Phi_0$  are the magnetic frustration in each loop. Using  $\varphi_1, \varphi_2, \varphi_4$  as the independent degrees of freedom, the Lagrangian of the qubit reads [32]:

$$\begin{aligned} \mathcal{L}(\varphi_1, \varphi_2, \varphi_4, \dot{\varphi}_1, \dot{\varphi}_2, \dot{\varphi}_4) = & \frac{\varphi_0^2 C}{2} (r_1 \dot{\varphi}_1^2 + r_2 \dot{\varphi}_2^2 + (r_4 + r_5) \dot{\varphi}_4^2 + r_3 (\dot{\varphi}_1 + \dot{\varphi}_2 + \dot{\varphi}_4)^2) + \\ & E_J (r_1 \cos \varphi_1 + r_2 \cos \varphi_2 + r_4 \cos \varphi_4 + r_3 \cos(-2\pi f_\epsilon - \varphi_1 - \varphi_2 - \varphi_4) + r_5 \cos(-2\pi f_\beta - \varphi_4)). \end{aligned} \quad (\text{S3})$$

Here we defined the reduced flux quantum  $\varphi_0 = \Phi_0/2\pi$ ,  $C$  is the capacitance of junction with size  $r = 1$ ,  $E_J = I_C \varphi_0$ . The canonical momenta  $q_i = \partial \mathcal{L} / \partial \dot{\varphi}_i$  are related to the derivative of

the conjugate phase operator:

$$\begin{pmatrix} \dot{\varphi}_1 \\ \dot{\varphi}_2 \\ \dot{\varphi}_4 \end{pmatrix} = \frac{1}{W} \begin{pmatrix} r_3(r_4 + r_5) + r_2(r_3 + r_4 + r_5) & -r_3(r_4 + r_5) & -r_3r_2 \\ -r_3(r_4 + r_5) & r_3(r_4 + r_5) + r_1(r_3 + r_4 + r_5) & -r_3r_1 \\ -r_3r_2 & -r_3r_1 & r_2r_3 + r_1(r_2 + r_3) \end{pmatrix} \begin{pmatrix} q_1 \\ q_2 \\ q_4 \end{pmatrix}, \quad (\text{S4})$$

where  $W = (C\varphi_0^2) \det(K)$ ,  $\det(K) = (r_2r_3(r_4 + r_5) + r_1(r_3(r_4 + r_5) + r_2(r_3 + r_4 + r_5)))$  is the dimensionless determinant of the capacitance matrix. We can now write down the Hamiltonian following a Legendre transformation  $\mathcal{H} = \sum_i q_i \dot{\varphi}_i - \mathcal{L}$ :

$$\begin{aligned} \mathcal{H} = & \frac{4E_C}{r_2r_3(r_4 + r_5) + r_1(r_3(r_4 + r_5) + r_2(r_3 + r_4 + r_5))} (n_1^2(r_3(r_4 + r_5) + r_2(r_3 + r_4 + r_5)) + \\ & n_2^2(r_3(r_4 + r_5) + r_1(r_3 + r_4 + r_5)) + n_4^2(r_2r_3 + r_1(r_2 + r_3)) - 2n_1n_2r_3(r_4 + r_5) - 2n_4r_3(r_1n_2 + r_2n_1)) - \\ & E_J(r_1 \cos \varphi_1 + r_2 \cos \varphi_2 + r_4 \cos \varphi_4 + r_3 \cos(-2\pi f_\epsilon - \varphi_1 - \varphi_2 - \varphi_4) + r_5 \cos(-2\pi f_\beta - \varphi_4)). \end{aligned} \quad (\text{S5})$$

Here we defined the quantized charge operator  $n_i = \hbar q_i$  as well as the charging energy  $E_C = e^2/2C$ . If we set  $f_\beta = 0$  the last term in the Josephson energy becomes  $r_5 \cos \varphi_4$ , which combined with the  $r_4$  term becomes an effective junction of size  $(r_4 + r_5)$ . For  $f_\beta = 0.5$ , the last term becomes  $-r_5 \cos \varphi_4$ , which now leads to an effective junction of size  $(r_4 - r_5)$ . Therefore we can tune the effective size of the coupling junction without affecting much of the rest of the qubit Hamiltonian. The different junction size will unavoidably lead to modifications of the qubit splitting.

In order to diagonalize the Hamiltonian it is convenient to find its representation in the charge basis  $\{|n\rangle\}$  where the Josephson terms have a simple expression, since [32]

$$\cos \varphi |n\rangle = \frac{e^{i\varphi} + e^{-i\varphi}}{2} |n\rangle = \frac{|n-1\rangle + |n+1\rangle}{2}. \quad (\text{S6})$$

The Josephson terms are therefore not represented by a closed Hilbert subspace in the charge basis. Therefore we need to restrict the number of charges between  $-n_{\max}$  and  $n_{\max}$  for each degree of freedom. Usually for  $n_{\max} = 10$  the error in the eigenenergies is less than 1%. Fig S1(b) shows the calculated qubit energies and wavefunctions for  $f_\beta = 0$  and  $f_\epsilon = 0.5$  using  $n_{\max} = 10$ .

### S1.1: Energy levels and Crosstalk

For a given set of fluxes  $(f_\epsilon, f_\beta)$  we can find the eigenenergies and eigenstates of the qubit. For all calculations shown in this section we take the values close to the experiment with the tunable coupling device  $r_1 = r_3 = 1.0, r_2 = 0.6, r_4 = 1.0, r_5 = 2.6, E_J/E_C = 70, E_J/h = 300$  GHz,  $n_{\max} = \pm 10$ . The areas of the two qubit loops are seen to be  $A_\epsilon/A_\beta \simeq 8.3$ , which agree with the data as seen in the calculations of Fig. 4(b) of the main text. In order to reproduce the experimental spectra we sweep the flux in the  $\epsilon$ -loop and assume the flux in the beta loop to be proportional to it,  $\Phi_\beta = \Phi_\epsilon/8.3$ .

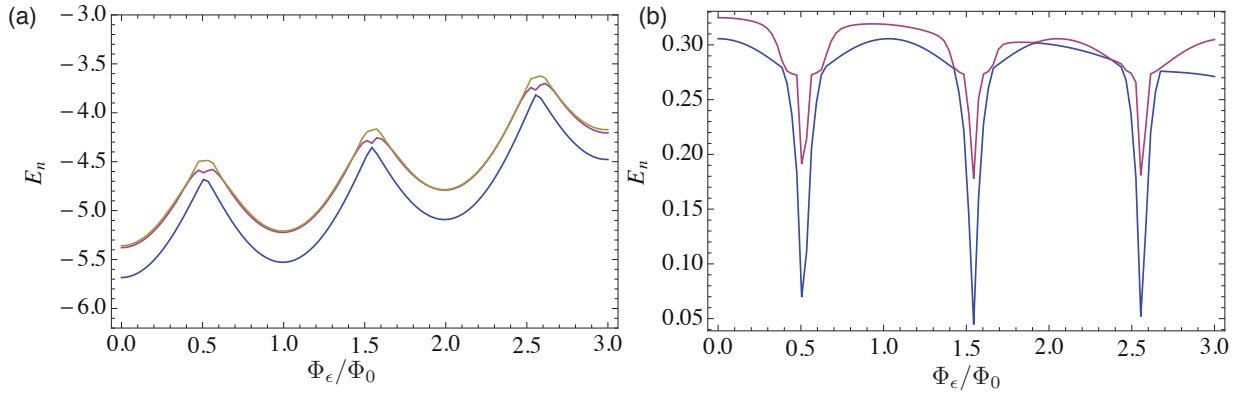


FIG. S2. (a) Calculated three lowest energy levels of the Hamiltonian in Eq (S5) as function of  $\Phi_\epsilon$  taking into account that  $\Phi_\beta = \Phi_\epsilon/9.4$ . The energies are in units of  $E_J$ . (b) Energy differences with respect to the ground state energy. Notice that qubit symmetry points are not falling on top of  $\Phi/\Phi_0 = 0.5$  due to the interference between the two qubit loops.

The resulting spectra in Fig. S2 clearly show a lack of periodicity, as would be the case for a qubit with no SQUID-loop. The qubit symmetry points do not agree with  $\Phi_\epsilon = \Phi_0(1/2+n)$ ,  $n$  being an integer. The difference is due to the interference between the two qubit loops. The potential energy terms related to the applied fluxes are

$$r_4 \cos(-2\pi f_\epsilon - \varphi_1 - \varphi_2 - \varphi_3) + r_5 \cos(-2\pi(f_\beta + f_\epsilon) - \varphi_1 - \varphi_2 - \varphi_3). \quad (\text{S7})$$

In analogy with the usual flux qubit potential [26], we can rewrite these terms as an effective new Josephson term  $\tilde{U}$  with effective critical current  $\tilde{I}$  and effective flux  $\tilde{f}$  as  $\tilde{U}/E_J = -\tilde{I} \cos(-\varphi_1 - \varphi_2 - \varphi_4 + 2\pi\tilde{f})$ . Expanding the cosine terms, we can relate  $\tilde{f}$  and  $\tilde{I}$  with the

rest of parameters:

$$- \tilde{U}/E_J = \tilde{I}(\cos \varphi_\Sigma \cos 2\pi \tilde{f} - \sin \varphi_\Sigma \sin 2\pi \tilde{f}), \quad (\text{S8})$$

$$= \cos \varphi_\Sigma (r_4 \cos 2\pi f_\epsilon + r_5 \cos(2\pi(f_\epsilon + f_\beta))) - \sin \varphi_\Sigma (r_4 \sin 2\pi f_\epsilon + r_5 \sin 2\pi(f_\epsilon + f_\beta)), \quad (\text{S9})$$

where  $\varphi_\Sigma = \varphi_1 + \varphi_2 + \varphi_3$ . In particular, at the symmetry point  $\tilde{f} = 1/2$  which cancels the second term in Eq. (S8). This implies that the term multiplying  $\sin \varphi_\Sigma$  has to be zero, leading to a transcendental equation to obtain the location of all symmetry points:

$$- \frac{r_4}{r_5} = \frac{\sin 2\pi f_\epsilon}{\sin 2\pi(f_\epsilon + f_\beta)}. \quad (\text{S10})$$

In addition to equation (10) we also impose the condition  $\cos(2\pi \tilde{f}) = -1$ , that is

$$-1 = r_4 \cos 2\pi f_\epsilon + r_5 \cos 2\pi(f_\epsilon + f_\beta). \quad (\text{S11})$$

We calculate the difference between consecutive qubit symmetry points in Fig. S3(a) over a period of  $\Phi_\beta$ . The cosine-like modulation clearly shows the interference between the two loops. The experimentally measured difference in periodicity of the qubit symmetry points is plotted in Fig. S3(b). A modulation of the periodicity is also clear. The relative change of periodicity of  $\sim 10\%$  agrees with the prediction of Eqs. (S10), (S11). Fig. S3(b) is scaled to the value at  $\Phi_\beta/\Phi_0 = 0$ . Fig. S3(a) is scaled such that “1” in the vertical axis would correspond to  $\Phi_\epsilon/\Phi_0 = 0.5$ .

The qubit Lagrangian shown here does not include geometric capacitance between islands and to ground. We have inspected the effect of those terms and found less than 10% variation in the qubit frequency.

### S1.2: Coupling operator

As shown in Ref. [33], the coupling strength of a flux qubit sharing a junction with a resonator or a transmission line is given by the modulus of matrix element of the phase operator across the coupling junction  $|\langle \hat{\varphi} \rangle|$ . In the circuit of Fig. S1 this corresponds to the phase across  $\hat{\varphi}_4$ . The coupling operator can be expressed in the qubit basis states using that the representation in the charge basis of the phase operator is

$$\langle n|\varphi|m\rangle = \frac{1}{2\pi} \int_{-\pi}^{\pi} \varphi e^{-i(m-n)\varphi} d\varphi = \begin{cases} 0 & \text{if } m = n, \\ -i \frac{(-1)^{(m-n)}}{m-n} & \text{if } m \neq n. \end{cases} \quad (\text{S12})$$



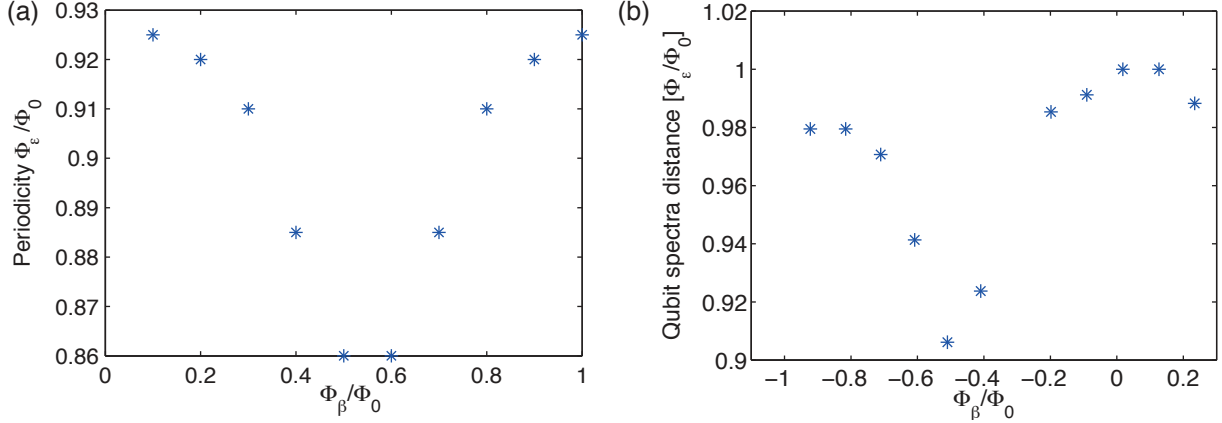


FIG. S3. (a) Calculated difference in consecutive qubit symmetry points as function of flux in  $\epsilon$ -loop, using Eqs. (S10), (S11). (b) Experimentally measured distance between qubit periods in units of coil driving voltage. The relative change of period  $\sim 10\%$  for both plots (a) and (b) agrees quite well. The difference at  $\Phi_\beta/\Phi_0 = 0$  and  $\Phi_\beta/\Phi_0 \simeq -1$  could be attributed to small flux drifts, given that the sweep is over many periods of flux for the qubit  $\epsilon$ -loop.

The limits of integration fall within a unit cell of the qubit potential. The qubit eigenstates are superpositions of charge states  $|g\rangle = \sum_{n_1, n_2, n_4 = -n_{max}}^{n_{max}} c_{n_1, n_2, n_4} |n_1, n_2, n_4\rangle$ . Therefore the matrix elements of the phase operator in the qubit basis  $\{|g\rangle, |e\rangle\}$  look like:

$$\langle M|\varphi_4|N\rangle = \sum_{n_1, n_2, n_4}^{n_{max}} \sum_{n'_1, n'_2, n'_4}^{n_{max}} c_{n_1, n_2, n_4}^* c_{n'_1, n'_2, n'_4} \left[ -i \frac{(-1)^{(n'_4 - n_4)}}{n'_4 - n_4} \delta_{n_1, n'_1} \delta_{n_2, n'_2} \right]. \quad (\text{S13})$$

We use the representation of the phase operator in the qubit basis to obtain the different components of the qubit operator. We want only transverse coupling,  $\langle\varphi_4\rangle \sim \sigma_x$  and not  $\sigma_z$  terms that would otherwise induce dephasing in the qubit from the line. Using equation (S13) we can compute the form of the operator, shown in Fig. S4

Clearly, the coupling operator only has  $\sigma_x$  component at the symmetry point, while its magnitude increases by approximately a factor of 2.6, as expected due to the modulation of the size of the  $\beta$ -junction. The qubit gap is also modulated as expected due to the effective change in size of  $\beta$ . The change is approximately of a factor of 2. Therefore the normalized coupling  $\Gamma/\Delta \sim |\langle\varphi_\beta\rangle|^2/\Delta$  increases by a factor of  $\sim 13.7$  from  $\Phi_\beta = 0$  to  $\Phi_\beta = \Phi_0/2$ . On Fig. S4(b) we also calculate the terms of the qubit Hamiltonian and coupling operator near  $\Phi_\epsilon = \Phi_0$  for fixed  $\Phi_\beta = 0$ . Clearly the coupling rotates from  $\sigma_x$  to  $\sigma_z$  as the qubit Hamiltonian rotates from  $\sigma_z$  to  $\sigma_x$ . Therefore the rotation of the coupling operator is exclusively due to

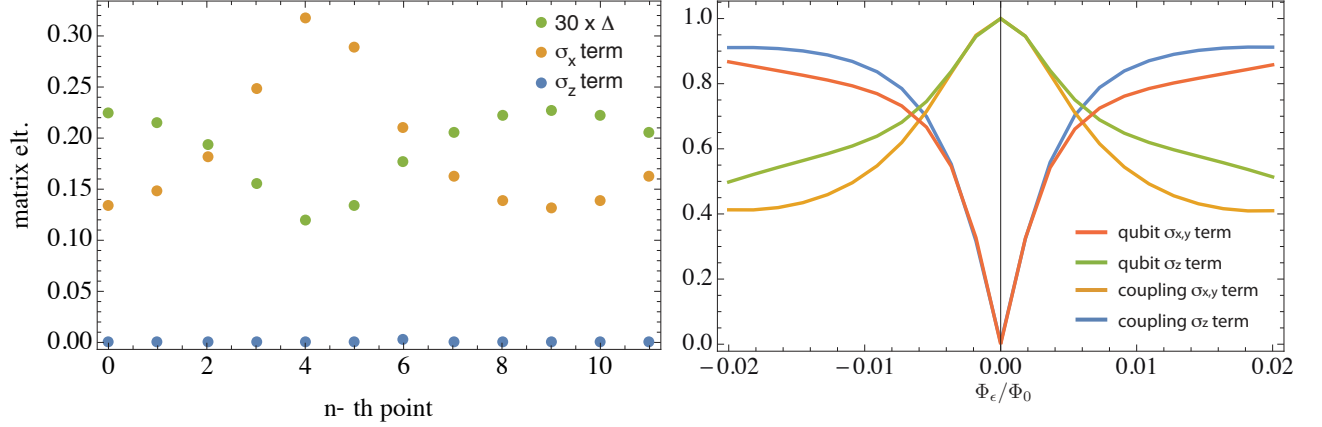


FIG. S4. (a) Calculated phase operator in the qubit basis at the symmetry point for different periods of  $\Phi_\epsilon$ . The operator has only  $\sigma_x$  component (orange) and no  $\sigma_z$  component (blue). The qubit splitting  $\Delta$  is also plotted, its value changing approximately a factor of 2 for the parameters of the device. (b) Calculated qubit Hamiltonian terms and coupling operator terms as function of  $\Phi_\epsilon$  for fixed  $\Phi_\beta = 0$ . Away from the symmetry point the qubit Hamiltonian rotates from  $\sigma_z$  and starts to acquire a  $\sigma_{x,y}$  component. The coupling operator follows closely the qubit Hamiltonian rotation. Therefore near the symmetry point the coupling operator rotates due to the qubit basis rotation as function of magnetic flux  $\Phi_\epsilon$  and not due to other terms in the Hamiltonian.

the qubit Hamiltonian rotation and not from other terms. Similar rotations of the coupling operator between qubits and transmission lines or resonators were already identified in [34].

## S2: SCATTERING RATES AT FINITE TEMPERATURE

Following from [35], the general definition of the master equation is

$$\dot{\rho}(t) = -\frac{i}{\hbar}[\mathcal{H}, \rho(t)] + \frac{1}{2} \sum_n [2C_n \rho(t) C_n^\dagger - \rho(t) C_n^\dagger C_n - C_n^\dagger C_n \rho(t)], \quad (\text{S14})$$

where the  $C_n = \sqrt{\gamma} A_n$  are the jump operators, with  $\gamma$  the rate for each process with collapse operator  $A_n$ . Here  $\mathcal{H}$  is the free Hamiltonian and contains the qubit part truncated to two levels,  $\mathcal{H}_{\text{qb}}/\hbar = \Delta \sigma_x/2 - \epsilon \sigma_z/2$  and the external driving  $\mathcal{H}_d/\hbar = 2\Omega \sin \omega_d t$ . For a qubit, the decay operator is  $\sigma_-$  while the excitation operator is  $\sigma_+$ . In terms of components, the diagonal decay terms of the master equation read

$$\dot{\rho}_{ii} = \sum_{j \neq i} (\Gamma_{ji} \rho_{jj} - \Gamma_{ij} \rho_{ii}). \quad (\text{S15})$$

Here  $\Gamma_{eg} = \Gamma_1(1 + n_{\text{th}})$  is the relaxation rate and  $\Gamma_{ge} = n_{\text{th}}\Gamma_1$  the excitation rate.  $n_{\text{th}}$  is the expectation value of photon number for a thermal state in equilibrium with a bath at temperature  $T$ :

$$n_{\text{th}} = \frac{1}{e^{\hbar\omega/k_B T} - 1}.$$

The off-diagonal decay terms take the form (for  $i \neq j$ )

$$\dot{\rho}_{ij} = -\gamma_{ij}\rho_{ij}, \quad (\text{S16})$$

where the decoherence rates are  $\gamma_{eg} = \Gamma_\varphi + \frac{1}{2}(\Gamma_{eg} + \Gamma_{ge}) = \Gamma_\varphi + (\Gamma_1/2)(1 + 2n_{\text{th}}) \equiv \Gamma_2$ , with  $\Gamma_\varphi$  the pure dephasing rate.

Explicitly, the decay equations for the four components of the density matrix now look:

$$\dot{\rho}_{ee} = \Gamma_{ge}\rho_{gg} - \Gamma_{eg}\rho_{ee} = n_{\text{th}}\Gamma_1(\rho_{gg} - \rho_{ee}) - \Gamma_1\rho_{ee}, \quad (\text{S17})$$

$$\dot{\rho}_{gg} = \Gamma_{eg}\rho_{ee} - \Gamma_{ge}\rho_{gg} = n_{\text{th}}\Gamma_1(\rho_{ee} - \rho_{gg}) + \Gamma_1\rho_{ee}, \quad (\text{S18})$$

$$\dot{\rho}_{eg} = -\gamma_{eg}\rho_{eg} = -[\Gamma_\varphi + \Gamma_1(1 + 2n_{\text{th}})/2]\rho_{eg} = -\Gamma_2\rho_{eg}, \quad (\text{S19})$$

$$\dot{\rho}_{ge} = -\gamma_{ge}\rho_{ge} = -[\Gamma_\varphi + \Gamma_1(1 + 2n_{\text{th}})/2]\rho_{ge} = -\Gamma_2\rho_{ge}. \quad (\text{S20})$$

The free evolution terms given by the commutator  $[\mathcal{H}, \rho(t)]$  can be easily computed in the rotating frame of the drive frequency  $\omega_d$ , under the rotating-wave approximation, where

$$\mathcal{H}/\hbar = -\delta\omega\sigma_z/2 + \Omega\sigma_x/2. \quad (\text{S21})$$

The detuning is defined as  $\delta\omega = \omega_d - \omega_{\text{qb}}$ ,  $\omega_{\text{qb}} = \sqrt{\Delta^2 + \epsilon^2}$  is the qubit energy splitting in units of angular frequency.  $\epsilon$  is the magnetic field energy controlled by  $\Phi_\epsilon$  (Fig. S1(a)). The full equation of motion for all components of the density matrix are:

$$\dot{\rho}_{ee} = -\frac{i\Omega}{2}(\rho_{ge} - \rho_{eg}) + n_{\text{th}}\Gamma_1(\rho_{gg} - \rho_{ee}) - \Gamma_1\rho_{ee}, \quad (\text{S22})$$

$$\dot{\rho}_{gg} = +\frac{i\Omega}{2}(\rho_{ge} - \rho_{eg}) + n_{\text{th}}\Gamma_1(\rho_{ee} - \rho_{gg}) + \Gamma_1\rho_{ee} = -\dot{\rho}_{ee}, \quad (\text{S23})$$

$$\dot{\rho}_{eg} = -\frac{i\Omega}{2}(\rho_{gg} - \rho_{ee}) - i\delta\omega\rho_{eg} - \Gamma_2\rho_{eg}, \quad (\text{S24})$$

$$\dot{\rho}_{ge} = +\frac{i\Omega}{2}(\rho_{gg} - \rho_{ee}) + i\delta\omega\rho_{ge} - \Gamma_2\rho_{ge}. \quad (\text{S25})$$

Now we want to find the steady-state populations of the qubit,  $\dot{\rho} = 0$ . The off-resonant terms are related by

$$\rho_{eg}(i\delta\omega + \Gamma_2) = \rho_{ge}(i\delta\omega - \Gamma_2). \quad (\text{S26})$$

Adding Eqs. (S22), (S25),

$$\Gamma_1 \rho_{ee} = -\rho_{ge} \left( \frac{i\Omega}{2} \right) \left( \frac{2\Gamma_2}{\Gamma_2 + i\delta\omega} + (\Gamma_2 - i\delta\omega)\Gamma_1 n_{\text{th}} \left( \frac{2}{\Omega} \right)^2 \right). \quad (\text{S27})$$

Using that  $\text{Tr}(\rho) = 1 = \rho_{ee} + \rho_{gg}$ , Eq. S23 can be rewritten as

$$\rho_{ee} = \frac{1}{\Gamma_1(1 + 2n_{\text{th}})} \left( \Gamma_1 n_{\text{th}} - i\frac{\Omega}{2}(\rho_{ge} - \rho_{eg}) \right). \quad (\text{S28})$$

Combining Eqs. (S26)-(S28) directly gives the solution for  $\rho_{ge}$ :

$$\rho_{ge} = \frac{i\Omega}{2} \frac{\Gamma_1(\Gamma_2 + i\delta\omega)}{\Gamma_2\Omega^2 + \Gamma_1(\Gamma_2^2 + \delta\omega^2)(1 + 2n_{\text{th}})}. \quad (\text{S29})$$

Using Eq. (S26) provides  $\rho_{eg}$ :

$$\rho_{eg} = -\frac{\Omega}{2\Gamma_2} \frac{i + \delta\omega/\Gamma_2}{(1 + (\delta\omega/\Gamma_2)^2)(1 + 2n_{\text{th}}) + \Omega^2/(\Gamma_1\Gamma_2)}. \quad (\text{S30})$$

Following [36], the reflection coefficient is defined as  $r \equiv -i(\Gamma_1/\Omega)\langle\sigma_-\rangle$ . It is easy to see that  $\langle\sigma_-\rangle = \rho_{eg}$ .

Therefore adding finite temperature to the system modifies the scattering parameters as follows:

$$r = r_0 \frac{(-1 + i\delta\omega/\Gamma_2)}{1 + \left(\frac{\delta\omega}{\Gamma_2}\right)^2 + \frac{\Omega_R^2}{\Gamma_1\Gamma_2}}, \quad (\text{S31})$$

with  $r_0 = \Gamma_1/(\Gamma_2(1 + 2n_{\text{th}}))$ . The form of Eq. (S31) is the same as the usual reflection coefficient if  $n_{\text{th}} = 0$ . Therefore the fitted values for  $r_0$  and  $\Gamma_2$  are going to be independent of temperature, the difference will appear in  $\Gamma_1$  and  $\Gamma_\varphi$ . The transmission coefficient will be given by  $t = 1 + r$

$$t = 1 + r = \frac{1 + (\delta\omega/\Gamma_2)^2 + r_0(-1 + i\delta\omega/\Gamma_2) + \frac{\Omega_R^2}{\Gamma_1\Gamma_2}}{1 + (\delta\omega/\Gamma_2)^2 + \frac{\Omega_R^2}{\Gamma_1\Gamma_2}}. \quad (\text{S32})$$

The minimum of transmission on-resonance when the driving is weak  $\Omega_R^2 \ll \Gamma_1\Gamma_2$  is

$$t_{\text{min}} = \frac{4\Gamma_1 n_{\text{th}} + 2\Gamma_\varphi(1 + 2n_{\text{th}}) + 4\Gamma_1 n_{\text{th}}^2}{(1 + 2n_{\text{th}})(\Gamma_1 + 2\Gamma_\varphi + 2\Gamma_1 n_{\text{th}})}.$$

Setting  $n_{\text{th}} = 0$  one restores the result of  $t_{\text{min}}(n_{\text{th}} = 0) = \Gamma_\varphi/\Gamma_2 = \Gamma_\varphi/(\Gamma_1/2 + \Gamma_\varphi)$ .

The extracted values of  $\Gamma_1$  from the experiment can be then bound assuming no thermal photons (lower bound) or the maximum number of photons allowed if  $\Gamma_\varphi = 0$  (upper bound), as seen in Fig. S5

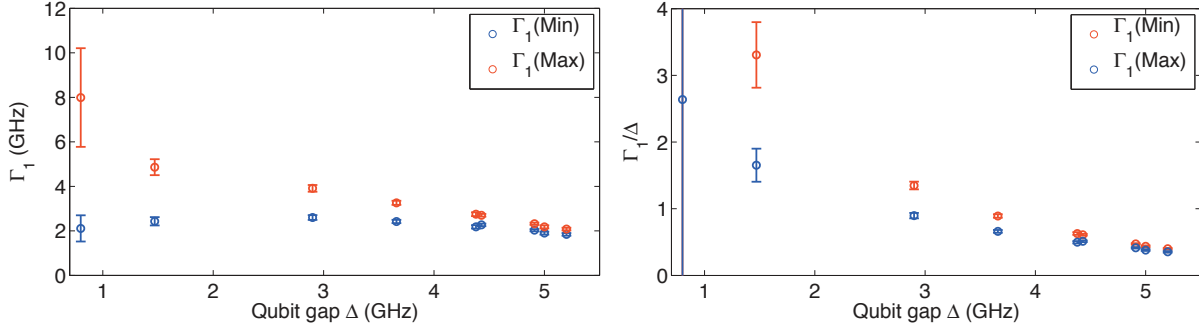


FIG. S5. (a)  $\Gamma_1$  as function of qubit gap  $\Delta$ , which corresponds to a different coupling rate. (b)  $\Gamma_1/\Delta$  as function of  $\Delta$ .

### S3: COMBINED FITTING OF $\text{RE}(T)$ AND $\text{IM}(T)$

The fits on figures 2, 3 of the main text are performed simultaneously on both the real and imaginary parts. We show here the total fitted transmission components. Fig. S6 corresponds to the fits of the tunable device while Fig. S7 corresponds to the devices with fixed coupling. As explained in the main text, even though the extracted emission rates correspond to the regime where the rotating-wave approximation (RWA) is not valid, by rotating the basis of the system Hamiltonian using a polaron transformation [37] the functional form of the real and imaginary parts of the transmission follow the same analytical form as the RWA case, with a renormalized qubit splitting  $\Delta$  and emission rate  $\Gamma_1$  instead. Due to the fact that most data is taken below the optimal bandwidth of our amplifier and circulators below 4 GHz, the quality of the fits degrades as the system enters the regime  $\Gamma_1 > \Delta$  (plots (g), (h), (i) in Fig. S6). The only relevant parameters extracted are  $r_0$  and  $\Gamma_2$ . As explained in the main text,  $r_0$  and  $\Gamma_2$  are enough to set bounds on  $\Gamma_1$  and the effective temperature of the system.

### S4: ESTIMATES OF DEPHASING RATE

The SQUID loop in the qubit with tunable coupling may be an additional source of decoherence, especially dephasing noise since fluctuations in the flux  $\Phi_\beta$  will directly convert into fluctuations of the qubit gap  $\Delta$ . We have assumed in the main text that the enhanced linewidth of the qubit is due to thermal effects. The justification is made here where we put bounds on possible sources of dephasing.

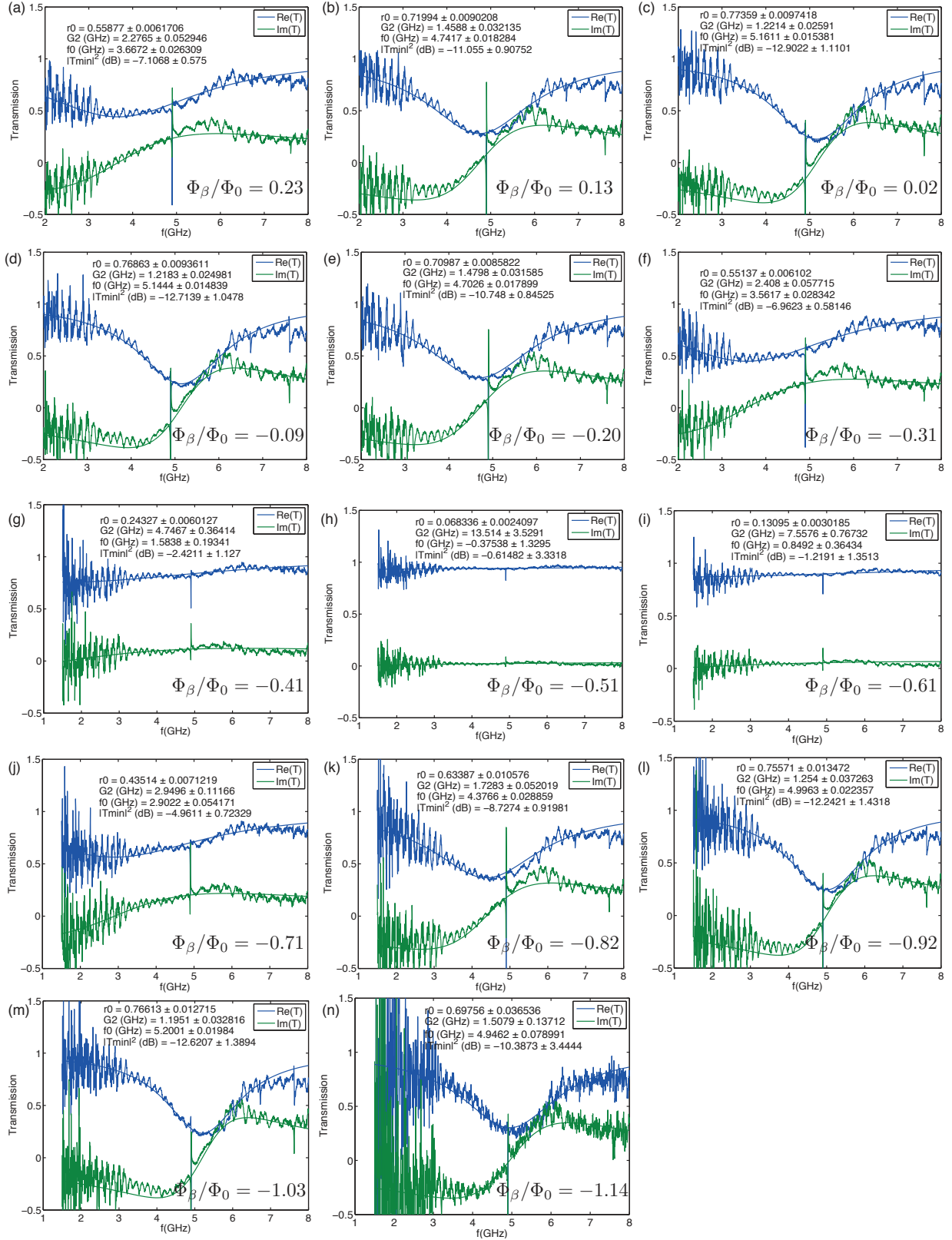


FIG. S6. (a)-(n) Combined fits corresponding to data in Fig. 3 from the main text.

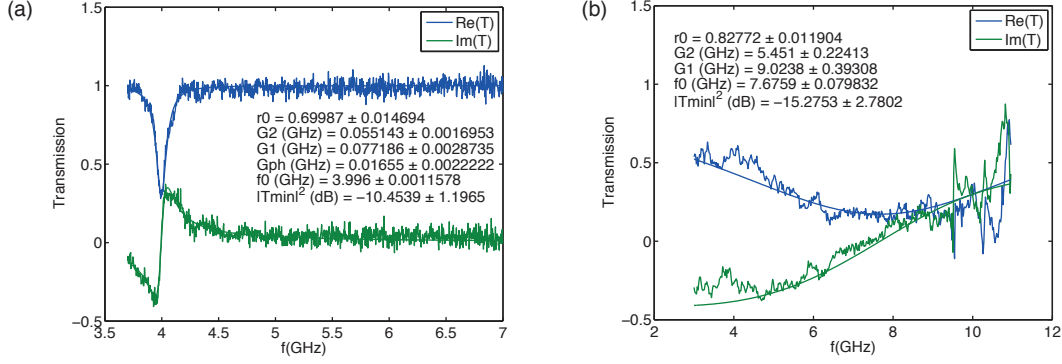


FIG. S7. Combined fits from devices with fixed coupling from Fig. 2 of the main text (a)  $\beta = 3.5$ , (b)  $\beta=1.8$ .

The sensitivity of the qubit gap as function of  $\Phi_\beta$  can be estimated by using the modulation of the qubit gap curve on Fig. 4 of the main text. An upper bound for the flux sensitivity is  $d\Delta/d\Phi_\beta \sim 7.4 \text{ GHz}/\Phi_0$ . Comparing this number to the sensitivity of the qubit to flux  $\Phi_\epsilon$ ,  $d\omega_{\text{qb}}/d\Phi_\epsilon \sim 5 \text{ GHz}/(2.5 \times 10^{-3}\Phi_0) \sim 2 \times 10^3 \text{ GHz}/\Phi_0$  we can see that sensitivity to flux noise in the  $\beta$ -loop is negligible.

Another possible source of flux noise would be through the qubit renormalization frequency as predicted by the spin-boson model. The model predicts [38] that the splitting of a two-level system in a bath of oscillators will be adiabatically renormalized to  $\Delta = \Delta_0(\Delta_0/\omega_C)^{\alpha_{\text{SB}}/(1-\alpha_{\text{SB}})}$ , where  $\omega_C$  is the cutoff frequency of the environment and  $\Delta_0$  is the bare qubit gap. Since  $\alpha_{\text{SB}} = \Gamma_1/\pi\Delta$  (see section S6) and therefore both  $\Gamma_1(\Phi_\beta)$ ,  $\Delta(\Phi_\beta)$ , fluctuations in  $\Phi_\beta$  may lead to fluctuations in  $\Delta$ . The sensitivity can be calculated:

$$\frac{\partial\Delta}{\partial\Phi_\beta} = \left(\frac{\Delta_0}{\omega_C}\right)^{\frac{\alpha_{\text{SB}}}{1-\alpha_{\text{SB}}}} \left[ 2\frac{d\Delta_0}{d\Phi_\beta} + \ln(\Delta_0/\omega_C)\frac{1}{(1-\alpha_{\text{SB}})^2}\frac{\Gamma'_1\Delta_0 - \Gamma_1\Delta'_0}{\Delta_0} \right] \simeq \left(\frac{\Delta_0}{\omega_C}\right)^{\frac{\alpha_{\text{SB}}}{1-\alpha_{\text{SB}}}} \frac{d\Delta_0}{d\Phi_\beta} \left[ 2 + \ln(\Delta_0/\omega_C)\frac{1+\alpha_{\text{SB}}}{(1-\alpha_{\text{SB}})^2} \right]. \quad (\text{S33})$$

Here we used that in our experiment (Fig. S5(a))  $\Gamma'_1 \equiv d\Gamma_1/d\Phi_\beta \approx -\Delta'_0 \equiv -d\Delta_0/d\Phi_\beta$ . The highest sensitivity occurs for  $\alpha_{\text{SB}} = 1/2$  where  $\partial\Delta/\partial\Phi_\beta \simeq -2(d\Delta_0/d\Phi_\beta)$ , assuming a worst case  $\Delta/\omega_C \sim 1/10$ . In the main text we find  $\Delta/\omega_C \sim 1/15$  as the worst case. Therefore this source of dephasing is also negligible.

## I. S5: TEMPERATURE SWEEPS

We want to establish more solid bounds on the maximum effective temperature  $T_{\text{eff}} = 90$  mK extracted from the fits of qubit spectra at different flux values, shown in Fig. S8(a), which complements the inferred  $n_{\text{tot}}$  in Fig. 3(f) of the main text. Here, we study the resonance on Fig. 3(a) from the main text, where the qubit frequency is highest, as function of the base temperature of our cryostat, which is where our device is thermalized to.

In Fig. S8(b) we show the extracted maximum photon number  $n_{\text{max}} = (1/2)(r_0^{1/2} - 1)$  and the corresponding effective temperature  $T_{\text{eff}} = (\hbar\Delta/k_B) \ln(1 + n_{\text{max}}^{-1})^{-1}$ . Clearly  $T_{\text{eff}}$  responds at all temperatures of the cryostat. Below  $\sim 30$  mK the effective temperature is  $T_{\text{eff}} = 90$  mK. Above  $\sim 80$  mK,  $T_{\text{eff}}$  increases at the same rate as the cryostat temperature, indicating that the chip temperature is now limited by the phonon bath of the mixing chamber. The data in Fig. S8(b) support the presence of an effective bath temperature of  $\sim 90$  mK when the cryostat is at the base temperature of  $T_B = 10$  mK, as was also inferred in Fig. S8(a) from the measurements of qubit spectra at different splittings. Other experiments with superconducting qubits have inferred similar effective temperatures [39].  $T_{\text{eff}}$  is therefore a good indication of the effective system temperature and justifies the observed changes in transmission for decreasing qubit splittings in Fig. 3 of the main text as having the origin in thermal effects and not dephasing.

We can also calculate the bounds on the qubit emission rate  $2\Gamma_2 r_0 < \Gamma_1 < 2\Gamma_2 \sqrt{r_0}$ , shown in Fig. S9(a), and the normalized coupling  $\Gamma_1/\Delta$  in Fig. S9(b). The average emission rate  $\Gamma_1$  remains constant up to 100 mK, while the average normalized coupling decreases slightly for increasing temperatures.

## S6: RELATION BETWEEN $\Gamma_1$ AND $\alpha_{\text{SB}}$

Let us begin with the spin-boson Hamiltonian

$$H = H_0 + H_{\text{int}} = \frac{\hbar\Delta}{2}\sigma_z + \sum_k \hbar\omega_k a_k^\dagger a_k + \sigma_x \sum_k g_k (a_k^\dagger + a_k), \quad (\text{S34})$$

which is characterized by the spectral function, defined as

$$J(\omega) = \frac{2\pi}{\hbar^2} \sum_k g_k^2 \delta(\omega - \omega_k) = \pi\omega\alpha_{\text{SB}}, \quad (\text{S35})$$



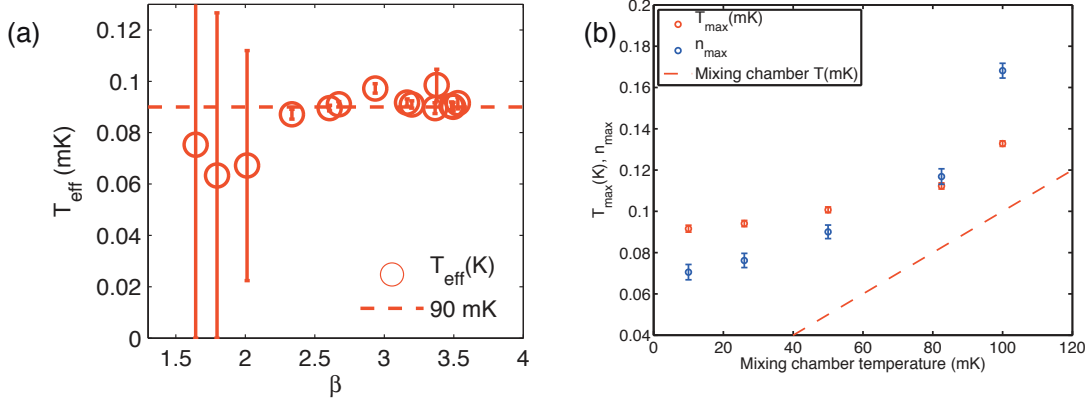


FIG. S8. (a) Calculated effective temperature from all qubit spectra in Fig. 3 of the main text. (b) Effective thermal photon number  $n_{\text{max}}$  (blue dots) and effective temperature (red dots) extracted from spectroscopy fits of qubit with tunable coupling resonances at bias flux where qubit has highest frequency  $\Delta/2\pi \sim 5.2$  GHz. Above cryostat temperatures of  $\sim 80$  mK the effective qubit temperature increases at the same rate as cryostat. Both sets of measurements support an effective temperature  $T_{\text{eff}}$  seen by the qubit of 90 mK.

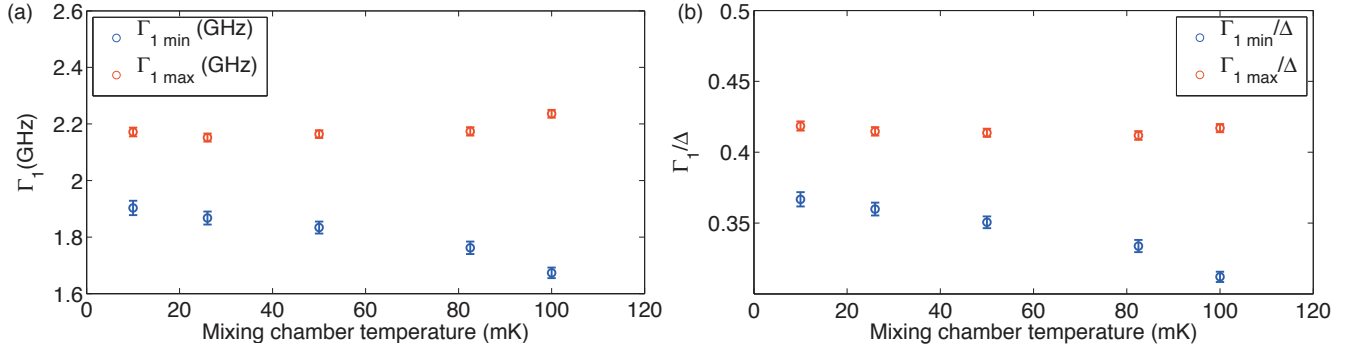


FIG. S9. (a) Calculated bounds on qubit emission rate  $\Gamma_1$  as function of temperature of cryostat. The average emission rate remains constant for the temperatures used. (b) Calculated bounds on normalized coupling  $\Gamma_1/\Delta$  of qubit to transmission line. The maximum coupling rate remains constant approximately while the average decreases.

where we have assumed an Ohmic spectral bath. As it is usual in condensed matter physics [38], [40], [6], we have expressed the spectral function  $J(\omega)$  as function of a dimensionless constant  $\alpha_{\text{SB}}$ , which characterizes the different quantum phases of the spin-boson model. More precisely, for  $\alpha_{\text{SB}} < 1/2$  the system is in the Markovian regime, for  $1/2 < \alpha_{\text{SB}} < 1$  the

system is in the overdamped regime, and for  $\alpha_{\text{SB}} > 1$  the system is in the localized phase. Note that our definition of  $J(\omega)$  differs from the one in [38] due to a factor of 1/2 that we omit in the last term of Eq. (S34).

Our aim in this section is to relate the qubit decay rate  $\Gamma_1$ , obtained from the master equation formalism, to the parameter  $\alpha_{\text{SB}}$ .

To this end, we will derive a quantum master equation for the qubit. We start from the combined qubit-bath density matrix in the interaction picture

$$\rho(t) = U(t)\rho_0U^\dagger(t), \quad (\text{S36})$$

where the unitary transformation  $U(t) = \exp(iH_0t)$  brings us into the rotating frame. This yields the following time-evolution equation for the density matrix  $\rho(t)$

$$\dot{\rho} = -\frac{i}{\hbar}[H_{\text{int}}, \rho(t)], \quad (\text{S37})$$

being  $H_{\text{int}}(t)$  the coupling Hamiltonian in the interaction picture, given by

$$\begin{aligned} H_{\text{int}}(t) &= U(t)H_{\text{int}}U(t)^\dagger \\ &= (\sigma_+e^{i\Delta t} + \sigma_-e^{-i\Delta t}) \sum_k g_k (a_k^\dagger e^{i\omega_k t} + a_k e^{-i\omega_k t}) \\ &= A(t)X(t), \end{aligned} \quad (\text{S38})$$

where  $A(t)$ ,  $X(t)$  are the system and bath operators, respectively.

Equation (S36) can be formally integrated, yielding the following integro-differential equation

$$\dot{\rho}(t) = \rho(0) - \frac{1}{\hbar^2} \int_0^t d\tau [H_{\text{int}}(t), [H_{\text{int}}(\tau), \rho(\tau)]]. \quad (\text{S39})$$

As it is commonplace, we assume the Born approximation (weak coupling to the bath, which allows us to approximate  $\rho(t) = \rho_{\text{sys}}(t) \otimes \rho_{\text{b}}(0)$ , for any time  $t$ ) and the Markov approximation (delta-correlated bath), which in turn corresponds with the Markovian dynamics of the spin-boson model defined by  $\alpha_{\text{SB}} < 1/2$  [37]. Under these conditions, we find a second-order differential equation for the reduced density matrix of the system

$$\dot{\rho}_{\text{sys}} = -\frac{1}{\hbar^2} \int_0^t d\tau \text{Tr}_{\text{b}}[H_{\text{int}}(t), [H_{\text{int}}(\tau), \rho_{\text{sys}}(\tau) \otimes \rho_{\text{b}}(0)]], \quad (\text{S40})$$

where  $\text{Tr}_{\text{b}}(A(t)X(t))$  refers to the trace over the bath degrees of freedom  $X(t)$ . Expanding the double commutator, and using the cyclic property of the trace,  $\text{Tr}(AX) = \text{Tr}(XA)$ , we can rewrite the master equation as

$$\dot{\rho}_{\text{sys}}(t) = \frac{\Gamma_1}{2}(2\sigma_- \rho_{\text{sys}}(t) \sigma_+ - \sigma_+ \sigma_- \rho_{\text{sys}}(t) - \rho_{\text{sys}}(t) \sigma_+ \sigma_-), \quad (\text{S41})$$

where the spontaneous decay rate  $\Gamma_1$  is given by

$$\begin{aligned}\Gamma_1 &= \frac{1}{\hbar^2} \int_{-\infty}^{\infty} d\tau e^{-i\Delta\tau} \langle [X(\tau), X(0)]_+ \rangle \\ &= \frac{1}{\hbar^2} \int_{-\infty}^{\infty} d\tau e^{-i\Delta\tau} \sum_k g_k^2 [(1+n_k)e^{i\omega_k\tau} + n_k e^{-i\omega_k\tau}].\end{aligned}\quad (\text{S42})$$

In eq. (S43), we have introduced the symetrized bath correlation function

$$\begin{aligned}\langle [X(\tau), X(0)]_+ \rangle &= \text{Tr}_b[(X(\tau)X(0) + X(0)X(\tau))\rho_b(0)] \\ &= \sum_k g_k^2 [(1+n_k)e^{i\omega_k\tau} + n_k e^{-i\omega_k\tau}],\end{aligned}\quad (\text{S43})$$

which can be readily calculated using the bosonic commutation relations  $[a_k, a_{k'}] = 0$ ,  $[a_k, a_{k'}^\dagger] = \delta_{kk'}$  and the two-time correlation functions

$$\begin{aligned}\langle a^\dagger(t)a(t') \rangle &= \sum_k g_k^2 n_k e^{i\omega_k(t-t')}, \\ \langle a(t)a^\dagger(t') \rangle &= \sum_k g_k^2 (1+n_k) e^{i\omega_k(t'-t)}.\end{aligned}\quad (\text{S44})$$

In the above expressions,  $n_k$  is the average number of photons in the  $k$ -th oscillator, and is given by

$$n_k = \frac{1}{\exp(\hbar\omega_k/k_B T) - 1}.\quad (\text{S45})$$

For the sake of simplicity, but without loss of generality, we will assume that we are at zero temperature, so that  $n_k = 0$ . Therefore, the relaxation rate  $\Gamma_1$  can be rewritten as

$$\begin{aligned}\Gamma_1 &= \frac{1}{\hbar^2} \int_{-\infty}^{\infty} d\tau e^{-i\Delta\tau} \sum_k g_k^2 e^{i\omega_k\tau} \\ &= \frac{1}{\hbar^2} \sum_k g_k^2 \int_{-\infty}^{\infty} d\tau e^{i(\omega_k - \Delta)\tau}.\end{aligned}\quad (\text{S46})$$

The last term in Eq. (S46) is nothing but the Fourier transform of the delta function

$$\delta(\omega_k) = \frac{1}{2\pi} \int_{-\infty}^{\infty} d\tau e^{i\omega_k\tau},\quad (\text{S47})$$

yielding the following expression for  $\Gamma_1$

$$\Gamma_1 = \frac{2\pi}{\hbar^2} \sum_k g_k^2 \delta(\Delta - \omega_k) = J(\Delta).\quad (\text{S48})$$

Using the second identity of Eq. (S34) we finally arrive at a relation between  $\Gamma_1$  and  $\alpha_{\text{SB}}$ ,

$$\Gamma_1 = \pi\alpha_{\text{SB}}\Delta.\quad (\text{S49})$$

It is worth mentioning that this result can be generalized for a bath at finite temperature  $T$  [40], [18], [41].

## S7: THE MAXIMUM COUPLING

As detailed in [33], a flux qubit coupled to a transmission line, sharing a junction, can be calculated from the case of coupling to a single-mode resonator. We derive here the expression of the coupling rate that is used in Fig. 4(a) of the main text to fit the experimental normalized coupling rate  $\Gamma_1/\Delta$ .

The quantized flux field in a 1D-transmission line assuming periodic boundary conditions (suitable for infinite transmission lines) takes the form

$$\hat{\phi} = \sum_k \sqrt{\frac{\hbar}{2c_0\omega_k L}} \left( \hat{a}_k e^{i(kx - \omega_k t)} + \hat{a}_k^\dagger e^{-i(kx - \omega_k t)} \right), \quad (\text{S50})$$

where the line has length  $L$ , capacitance and inductance per unit length  $c_0, l_0$  and mode frequency  $\omega_k$ . The dispersion relation is given by  $\omega_k = kc = k(l_0 c_0)^{-1/2}$ ,  $c$  being the speed of light in the line. The coupling term takes the form (see Supplementary material in [33]):

$$\hat{H}_{\text{int}} = \frac{1}{2l_0} \varphi_0 \hat{\varphi}_\beta \frac{\partial \hat{\phi}}{\partial x} \delta(x), \quad (\text{S51})$$

which is nothing but the current along the transmission line times the effective node flux generated by the qubit  $\varphi_0 \langle \hat{\varphi}_\beta \rangle$ , with  $\varphi_0 = \Phi_0/2\pi$  the reduced flux quantum and  $\hat{\varphi}_\beta$  the phase operator across the qubit coupling junction  $\beta$ .  $\delta(x)$  is the Dirac delta, since the qubit is assumed to sit at the origin  $x = 0$ . The strength of the coupling to mode  $k$  is given by

$$g_k = \frac{1}{2l_0} \varphi_0 \langle \hat{\varphi}_\beta \rangle \frac{1}{\sqrt{L}} \sqrt{\frac{\hbar \omega_k}{2c_0 c^2}}. \quad (\text{S52})$$

The spectral density  $J(\omega)$  [42], which as shown in section S6 corresponds to the spontaneous emission rate  $\Gamma_1$ , can be directly calculated

$$J(\omega) = 2\pi \sum_k (|g_k|/\hbar)^2 \delta(\omega - \omega_k) = 2\pi \sum_k \frac{1}{l_0^2} \frac{1}{L} \frac{\omega_k}{8\hbar c_0 c^2} \varphi_0^2 |\langle \hat{\varphi}_\beta \rangle|^2 \delta(\omega - \omega_k). \quad (\text{S53})$$

Taking the limit to the continuum, using that the density of states is  $2\pi/L$ ,

$$J(\omega) = 2 \int_0^\infty d\omega_k \frac{\omega_k}{8\hbar c_0 l_0^2 c^3} \varphi_0^2 |\langle \hat{\varphi}_\beta \rangle|^2 \delta(\omega - \omega_k) = \frac{\omega}{4\hbar Z_0} \varphi_0^2 |\langle \hat{\varphi}_\beta \rangle|^2, \quad (\text{S54})$$

$Z_0 = (l_0/c_0)^{-1/2}$  being the characteristic impedance of the transmission line. The factor of 2 in front of the integral is due to the fact that the frequency  $\omega_k$  is degenerate for wavenumbers  $k$  and  $-k$ . Therefore, and connecting to the traces on Fig. 4(a) of the main text, we can

express the reduced coupling  $\Gamma_1/\Delta$  as function of the expectation value of the phase operator and the impedance of the line:

$$\frac{J(\Delta)}{\Delta} = \frac{\Gamma_1}{\Delta} = \frac{1}{16e^2} \frac{\hbar}{Z_0} |\langle \hat{\varphi}_\beta \rangle|^2 = \frac{1}{8\pi} \frac{R_Q}{Z_0} |\langle \hat{\varphi}_\beta \rangle|^2, \quad (\text{S55})$$

where  $R_Q = h/(2e)^2 \simeq 6.5 \text{ k}\Omega$  is the resistance quantum. Equation (S55) indicates that in order to increase the coupling to its highest value,  $Z_0$  has to be as low as possible and  $|\langle \varphi_\beta \rangle|$  must be increased by making the  $\beta$ -junction size smaller and therefore having a phase drop of order 1 across it. Achieving  $\Gamma_1/\Delta \approx 10$  is therefore within reach. From this analysis the quantity  $\Gamma_1/\Delta$  can be understood as a normalized coupling strength.

## S8: FULL CIRCUIT LAYOUT

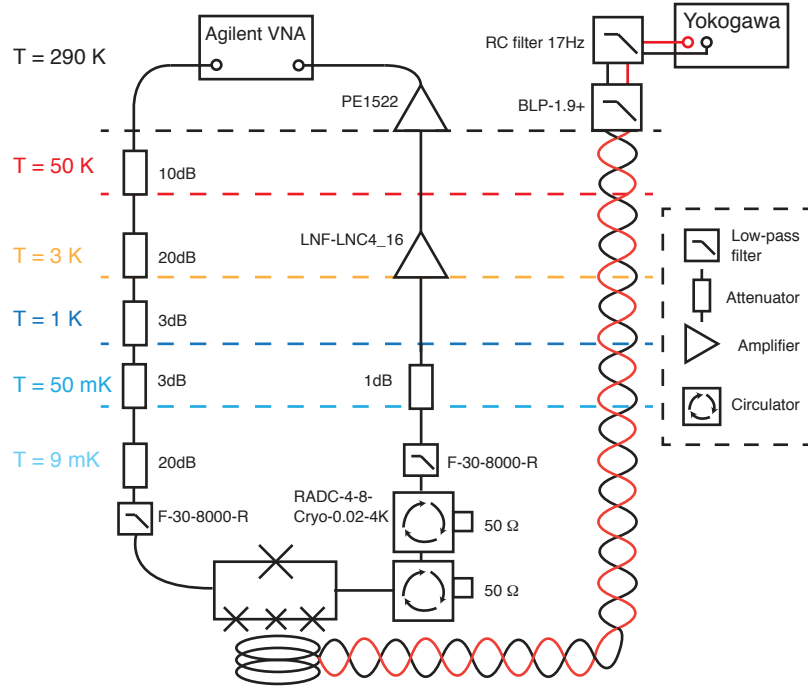


FIG. S10. Schematic of the full circuit for transmission measurements.

[1] Haroche, S., Raimond, J.-M. *Exploring the Quantum: Atoms, Cavities, and Photons (Oxford Graduate Texts)* (Oxford University Press, USA, 2006), first edition.

- [2] Wallraff, A., *et al.* Circuit Quantum Electrodynamics: Coherent Coupling of a Single Photon to a Cooper Pair Box. *Nature* **431**, 162 (2004).
- [3] Peropadre, B., Zueco, D., Porras, D., García-Ripoll, J. J. Nonequilibrium and nonperturbative dynamics of ultrastrong coupling in open lines. *Phys. Rev. Lett.* **111**, 243602 (2013).
- [4] Díaz-Camacho, G., Bermudez, A., García-Ripoll, J. J. Dynamical polaron ansatz: a theoretical tool for the ultra-strong coupling regime of circuit QED. *arXiv:1512.04244* (2015).
- [5] Leggett, A. J. *et al.* Dynamics of the dissipative two-state system. *Rev. Mod. Phys.* **59**, 1 (1987).
- [6] Le Hur, K. Kondo resonance of a microwave photon. *Phys. Rev. B* **85**, 140506 (2012).
- [7] Shen, J.-T., Fan, S. Coherent Single Photon Transport in a One-Dimensional Waveguide Coupled with Superconducting Quantum Bits. *Phys. Rev. Lett.* **95**, 213001 (2005).
- [8] Astafiev, O. *et al.* Resonance Fluorescence of a Single Artificial Atom. *Science* **327**, 840 (2010).
- [9] Kimble, H. J. The quantum internet. *Nature* **453**, 1023 (2008).
- [10] Hoi, I.-C. *et al.* Demonstration of a Single-Photon Router in the Microwave Regime. *Phys. Rev. Lett.* **107**, 073601 (2011).
- [11] García-Álvarez, L. *et al.* Fermion-fermion scattering in quantum field theory with superconducting circuits. *Physical Review Letters* **114**, 070502 (2015).
- [12] Hoi, I.-C. *et al.* Giant Cross-Kerr Effect for Propagating Microwaves Induced by an Artificial Atom. *Phys. Rev. Lett.* **111**, 053601 (2013).
- [13] van Loo, A. F. *et al.* Photon-Mediated Interactions Between Distant Artificial Atoms. *Science* **342**, 1494 (2013).
- [14] Tiecke, T. G. *et al.* Nanophotonic quantum phase switch with a single atom. *Nature* **508**, 241 (2014).
- [15] A. Goban, *et al.* Superradiance for atoms trapped along a photonic crystal waveguide. *Phys. Rev. Lett.* **115**, 063601 (2015).
- [16] Arcari, M. *et al.* Near-Unity Coupling Efficiency of a Quantum Emitter to a Photonic Crystal Waveguide. *Phys. Rev. Lett.* **113**, 093603 (2014).
- [17] Ciuti, C., Bastard, G., Carusotto, I. Quantum vacuum properties of the intersubband cavity polariton field. *Phys. Rev. B* **72**, 115303 (2005).
- [18] Gardiner, C., Zoller, P. *Quantum Noise* (Springer-Verlag Berlin Heidelberg, 2004).
- [19] Grifoni, M., Paladino, E., Weiss, U. Dissipation, decoherence and preparation effects in the

- spin-boson system. *Eur. Phys. J. B* **10**, 719 (1999).
- [20] Gammaitoni, L., Hänggi, P., Jung, P., Marchesoni, F. Stochastic resonance. *Rev. Mod. Phys.* **70**, 223 (1998).
- [21] Penttilä, J. S., Parts, U., Hakonen, P. J., Paalanen, M. A., Sonin, E. B. Superconductor-Insulator Transition in a Single Josephson Junction. *Phys. Rev. Lett.* **82**, 1004 (1999).
- [22] Sabín, C., Peropadre, B., Rey, M. D., Martín-Martínez, E. Extracting past-future vacuum correlations using circuit QED. *Phys. Rev. Lett.* **109**, 033602 (2012).
- [23] Sánchez-Burillo, E., Zueco, D., García-Ripoll, J. J., Martín-Moreno, L. Scattering in the Ultrastrong Regime: Nonlinear Optics with One Photon. *Phys. Rev. Lett.* **113**, 263604 (2014).
- [24] Niemczyk, T. *et al.* Circuit quantum electrodynamics in the ultrastrong-coupling regime. *Nat. Phys.* **6**, 772 (2010).
- [25] Forn-Díaz, P. *et al.* Observation of the Bloch-Siegert Shift in a Qubit-Oscillator System in the Ultrastrong Coupling Regime. *Phys. Rev. Lett.* **105**, 237001 (2010).
- [26] Mooij, J. E. *et al.* Josephson Persistent-Current Qubit. *Science* **285**, 1036 (1999).
- [27] Bourassa, J. *et al.* Ultrastrong coupling regime of cavity QED with phase-biased flux qubits. *Phys. Rev. A* **80**, 032109 (2009).
- [28] Orgiazzi, J. L. *et al.* Flux qubits in a planar circuit quantum electrodynamics architecture: quantum control and decoherence. *arXiv:1407.1346* (2014).
- [29] Peropadre, B. *et al.*, Scattering of coherent states on a single artificial atom. *New J. Phys.* **15**, 035009 (2013).
- [30] M. Haeberlein, *et al.*, *arXiv:1506.09114* (2015).
- [31] A. Fedorov, P. Macha, A. K. Feofanov, C. J. P. M. Harmans, and J. E. Mooij, *Phys. Rev. Lett.* **106**, 170404 (2011).
- [32] M. H. Devoret, “Quantum fluctuations (les houches session lxiii),” (Elsevier, 1997) pp. 351–386
- .
- [33] B. Peropadre, D. Zueco, D. Porras, and J. J. García-Ripoll, *Phys. Rev. Lett.* **111**, 243602 (2013).
- [34] B. Peropadre, P. Forn-Díaz, E. Solano, and J. J. García-Ripoll, *Phys. Rev. Lett.* **105**, 023601 (2010).
- [35] B. Peropadre, J. Lindkvist, I. C. Hoi, C. M. Wilson, J. J. Garcia-Ripoll, P. Delsing, and

- G. Johansson, *New Journal of Physics* **15**, 035009 (2013).
- [36] O. Astafiev, A. M. Zagoskin, A. A. Abdumalikov, Y. Pashkin, T. Yamamoto, K. Inomata, Y. Nakamura, and J. S. Tsai, *Science* **327**, 840 (2010).
- [37] G. Díaz-Camacho, A. Bermudez, and J. J. García-Ripoll, arxiv:1512.04244 (2015), arXiv:1512.04244.
- [38] A. J. Leggett, S. Chakravarty, A. T. Dorsey, M. P. A. Fisher, A. Garg, and W. Zwerger, *Reviews of Modern Physics* **59**, 1 (1987).
- [39] J. M. Fink, L. Steffen, P. Studer, L. S. Bishop, M. Baur, R. Bianchetti, D. Bozyigit, C. Lang, S. Filipp, P. J. Leek, and A. Wallraff, *Phys. Rev. Lett.* **105**, 163601 (2010).
- [40] U. Weiss, *Quantum Dissipative Systems*, 3rd ed. (World Scientific Publishing Company, 2008)
- .
- [41] A. Shnirman, Y. Makhlin, and G. Schön, *Physica Scripta* **2002**, 147 (2002).
- [42] A. O. Caldeira and A. J. Leggett, *Annals of Physics* **149**, 374 (1983).